

# Use of a multi-spectral camera in the characterization of skin wounds

Ali Basiri<sup>1</sup>, Marjan Nabili<sup>1</sup>, Scott Mathews<sup>1</sup>, Alex Libin<sup>2,3</sup>, Suzanne Groah<sup>2</sup>, Herke J. Noordmans<sup>4</sup>, Jessica C. Ramella-Roman<sup>1,2\*</sup>

<sup>1</sup>The Catholic University of America, Washington, D.C.

<sup>2</sup>National Rehabilitation Hospital, Washington, DC

<sup>3</sup>Georgetown University Medical Center, Washington, DC

<sup>4</sup>University Medical Center Utrecht, Utrecht, The Netherlands

\*ramella@cua.edu

**Abstract:** Skin breakdown is a prevalent and costly medical condition worldwide, with the etiologic and healing processes being complex and multifactorial. Quantitative assessment of wound healing is challenging due to the subjective measurement of wound size and related characteristics. We propose that in vivo spectral reflectance measurements can serve as valuable clinical monitoring tool/device in the study of wound healing. We have designed a multi spectral camera able to acquire 18 wavelength sensitive images in a single snapshot. A lenslets array in front of a digital camera is combined with narrowband filters (bandwidth 10 nm) ranging from 460 to 886nm. Images taken with the spectroscopic camera are composed of 18 identical sub-images, each carrying different spectral information, that can be used in the assessment of skin chromophores. A clinical trial based on a repeated measures design was conducted at the National Rehabilitation Hospital on 15 individuals to assess whether Poly Carboxy Methyl Glucose Sulfate (PCMGS, CACIPLIQ20), a bio-engineered component of the extracellular matrix of the skin, is effective at promoting healing of a variety of wounds. Multi spectral images collected at different wavelengths combined with optical skin models were used to quantify skin oxygen saturation and its relation to the traditional measures of wound healing.

©2010 Optical Society of America

OCIS codes: (110.4234) Multispectral and hyperspectral imaging; (170.1870) Dermatology

---

## References and links

1. A. Vogel, V. V. Chernomordik, J. D. Riley, M. Hassan, F. Amyot, B. Dasgeb, S. G. Demos, R. Pursley, R. F. Little, R. Yarchoan, Y. Tao, and A. H. Gandjbakhche, "Using noninvasive multispectral imaging to quantitatively assess tissue vasculature," *J. Biomed. Opt.* **12**, 051604.1–12 (2004).
2. G. N. Stamatias, M. Southall, and N. Kollias, "In vivo monitoring of cutaneous edema using spectral imaging in the visible and near infrared," *The society for investigative dermatology* **126**(8), 1753–1760 (2006).
3. H. J. Noordmans, R. De Roode, M. Staring, and R. Verdaasdonk, "Registration and analysis of in-vivo multi-spectral images for correction of motion and comparison in time," *Proc. SPIE*, **7**, 608106.1–9 (2006).
4. R. De Roode, H. J. Noordmans, R. Verdaasdonk, and V. Sigurdsson, "MULTISPECTRAL DETECTORS: Multispectral system evaluates treatments in dermatology," *Laser Focus World*, **42** (Apr 2006) [www.laserfocusworld.com](http://www.laserfocusworld.com).
5. T. Binzoni, A. Vogel, A. H. Gandjbakhche, and R. Marchesini, "Detection limits of multi-spectral optical imaging under the skin surface," *Phys. Med. Biol.* **53**(3), 617–636 (2008).
6. I. V. Meglinski, and S. J. Matcher, "Quantitative assessment of skin layers absorption and skin reflectance spectra simulation in the visible and near-infrared spectral regions," *Physiol. Meas.* **23**(4), 741–753 (2002).
7. I. V. Meglinski, and S. J. Matcher, "Computer simulation of the skin reflectance spectra," *Comput. Methods Programs Biomed.* **70**(2), 44–50 (2003).
8. J. Ramella-Roman, and S. Mathews, "Spectroscopic Measurement of Oxygen Saturation in the Retina," *IEEE J. Sel. Top. Quantum Electron.* **13**(6), 1697–1703 (2007).
9. S. A. Mathews, "Design and fabrication of a low-cost, multispectral imaging system," *Appl. Opt.* **47**(28), F71–F76 (2008).

#119304 - \$15.00 USD Received 29 Oct 2009; revised 13 Jan 2010; accepted 14 Jan 2010; published 1 Feb 2010

(C) 2010 OSA

15 February 2010 / Vol. 18, No. 4 / OPTICS EXPRESS 3244

10. J. Ramella - Roman, S. Mathews, H. Kandiamalla, A. Nabili, D. Duncan, S. A. D'Anna, S. M. Shah, and Q. D. Nguyen, "Measurement of oxygen saturation in the retina with a spectroscopic sensitive multi aperture camera," *Opt. Express* **16**(9), 6170–6182 (2008) (i).
11. T. Moffitt, Y. Chen, and S.A. Prahl. "Preparation and characterization of polyurethane optical phantoms," *J. Biomed. Opt.* **11** 041103.1–10 (2006).
12. L. H. Wang, S. L. Jacques, and L. Q. Zheng, "MCML--Monte Carlo modeling of light transport in multi-layered tissues," *Comput. Methods Programs Biomed.* **47**(2), 131–146 (1995).
13. G. N. Stamatas, and N. Kollias, "In vivo documentation of cutaneous inflammation using spectral imaging," *J. Biomed. Opt.* **12**(5), 051603 (2007).
14. S. Iyad, Saidi, 1992 Transcutaneous optical measurement of hyperbilirubinemia in neonates. Ph.D. dissertation, Rice University, Houston, TX, USA.
15. S. Takatani, and M. D. Graham, "Theoretical analysis of diffuse reflectance from a two-layer tissue model," *IEEE Trans. Biomed. Eng.* **BME-26**(12), 656–664 (1979).
16. Center for Wound Healing, and Hyperbaric Medicine, "Smoking and woundhealing," Wound Healing Center., Trinitas Hospital. (2001). <http://www.woundhealingcenter.org/SmokingandWoundHealing.pdf>. C. Ueno, T. Hunt, H. Hopf, "Using Physiology to improve surgical wound outcomes," *Plast. Reconstr. Surg.* **117**, 59S–71S (2006)
17. Some portions of this paper have appeared in M. Nabili, J. C. Ramella-Roman, Assessment of skin wound healing with a multi-aperture camera, *Photonics in Dermatology and Plastic Surgery*, Proceedings of SPIE Vol. 7161A, 2009.

## 1. Introduction

Spectroscopic imaging is a noninvasive technique used to monitor skin characteristics such as blood volume, tissue oxygen saturation, and in situ chromophore concentrations. Recently several authors have used spectroscopic imaging for assessment of skin diseases. Vogel *et al.* [1] used near-infrared spectroscopy (NIRS) to study the Kaposi's sarcoma (KS). Their system comprised six narrow-band optical filters (700, 750, 800, 850, 900 and 1000 nm), an automated filter wheel, and a CCD camera. The authors employed a best-fit, multi-variant analysis to estimate the concentrations of various chromophores in the tissue.

Stamatas *et al.* [2] monitored edema *in vivo* with a spectroscopic imaging system containing a custom made camera with 18 narrow band filters in range of 400 to 970nm and three broad band filters in red, green, and blue regions of the light spectrum. The concentration of oxygenated hemoglobin, deoxygenated hemoglobin, and water were calculated for each pixel, and used to construct oxygen saturation maps of the lesion. Skin erythema and skin edema were monitored over time.

Researchers at the Department of Clinical Physics at UMC Utrecht in the Netherlands [3,4], used multi-spectral imaging to capture a series of images in the wavelength range 400 to 720 nm with a narrowband liquid crystal tunable filter. This system was used for the detection and diagnosis of suspicious lesions on the skin, tumor detection and demarcation, and for visualizing oxygenation changes in the tissue.

Binzoni *et al.* [5] developed Monte Carlo models of light transfer into tissue as well as experiments of light propagation into tissue phantoms. The main concern of their study was to investigate the behavior of different wavelengths traveling inside skin tissue and its influence on the resulting spectral images. They argued that the depth that photons reach inside the tissue does not exceed 2 to 3 mm and that the information in a spectral image mostly reflects a small volume under each superficial pixel. The study follows the seven layers Meglinski and Matcher model [6,7] of skin with the added ability of inserting pathological tissue in the layered structure. The study ultimately shows that the image contrast depends on the depth and the type of chromophores in different molecules.

We have used a multi-spectral camera to monitor oxygen saturation in the retina non-invasively. This system was composed of a 6 wavelength camera in the visible region of the spectrum combined with a fundus ophthalmoscope [8,10].

Recently we have developed a similar system to monitor oxygen saturation in the skin. The experimental apparatus uses a lenslet array combined with a 12 bit camera to generate 18 images from the same area of the skin. Each lens is interfaced with a narrowband filter

bandwidth 10 nm) ranging from 480 to 886nm. The acquired images carry different spectral information that could be used in evaluation of skin chromophores.

A clinical trial was conducted at the National Rehabilitation Hospital on 15 subjects with 22 different wounds to assess the efficacy of Carboxy Methyl Glucose Sulfate (PCMGS) CACIPLIQ20® in the healing process of different types of skin wounds. The purpose of our study was to assess the efficacy of utilizing a multi-spectral camera to quantify critical skin metabolic parameters of oxygen saturation as a means to provide a more detailed description of wound status.

## 2. Material and methods

Multi-spectral images collected at various wavelengths were combined with different optical skin models, to quantify parameters of interest. Multi-spectral images are captured with an experimental imaging system, which can simultaneously acquire 18 wavelength-images on a single charge-coupled device (CCD, Fig. 1) [8,9]. Each of the sub-images could be independently filtered using narrow band-pass filters, polarizers, or neutral density filters. Filters could be changed in different experimental scenario. Since all sub-images were acquired simultaneously, motion artifacts due to patient motion or pulsatory motion could be dramatically reduced. The system hardware has been previously described [9,10], hence we will restate only its most fundamental aspects.

The system consisted of a monochromatic digital camera, (Lumenera, North Andover, MA, CCD dimensions 36.1mm × 24.0mm) with 4008 pixels × 2672 pixels. Images could be acquired either at 8 bit or re-mapped at 16 bit. The CCD, electronics and USB 2.0 interface were mounted in a light tight, black anodized aluminum housing. The multi-lens camera, with integrated illuminator was mounted on an articulating arm, so that it could be easily positioned during imaging sessions.

A custom-built lenslet array was mounted in front of the housing unit at ~0.5 mm from the CCD. The array was designed in a way to maximize each sub-image area by using most of the space available on the CCD. Each lens was separated by 0.6 cm center to center in the horizontal direction and 1.0 cm center to center in the vertical direction.

The lenses (Sunex, Inc., Carlsbad, CA) used in this system had a 5.9 mm focal length. Each lens position was adjustable so that they could be separately focused. The lens plate could accommodate 18 lenses and was a matched with a second supporting element that could house either filters or polarizing elements. 16 narrowband filters were matched to the lens plate and 2 polarizers.

The following band pass filters were chosen: 480, 500, 520, 530, 540, 560, 580, 590, 600, 620, 630, 640, 660, 680, 700, and 886 nm (Newport, Irvine, CA). Filters with center wavelengths below 650 nm had an additional IR-cut coating. The diversity of these filters was chosen based on our interest in skin optical properties. Two polarizers were added to the filters layout the polarizers were parallel and perpendicular to a source polarizer. In addition, a neutral density filter (OD = 1) covered the two polarizers to avoid saturation.

In order to magnify the imaging area of interest, two 7.5 cm diameter, plano-convex glass lenses with 15 cm focal length were mounted in a cylindrical aluminum support and attached to the camera housing. This method magnified the sub-images to the appropriate size. The light source was a filtered quartz halogen lamp (Labtek, Campbell, CA) connected to a ring illuminator, which was placed over the cylindrical aluminum support.

A polarizer was placed over the ring illuminator and oriented respectively parallel and perpendicular to the camera polarizers. A laptop (HP ProBook, Palo Alto, CA) was used to control the camera through USB 2.0 interface and the Lumenera acquisition software. The whole system was placed on a movable cart and, therefore, was easily transportable in clinical setting.



Fig. 1. An image of the clinical system apparatus

### 2.1 System calibration

To investigate the behavior of camera to different light densities and exposure times, a test was conducted using a 99.8% white reflectance standard (Labsphere, North Sutton, NH). During the test, the camera exposure times was changed from 0 to 100 ms. All test were done in a dark environment. A region of interest of 100 pixels x 100 pixels was sampled from the sub-image of 540 nm.

In order to measure camera linearity, the on board light source was fixed at a particulate power level, then the camera exposure time was changed from 0 to 1000 ms, for each exposure time an image was captured and the mean and standard deviation of a region of interest (20 x 20 pixels) was calculated. Different light power settings were also tested, with the same procedure. The test showed a linear behavior of the camera as long as the gamma setting was kept at 1. Linearity investigation was done for all wavelengths available in the filter array of the camera. For gamma = 1.5 a non-linear behavior was noticed for low light values. During the experimental work the gamma parameter was hence kept to 1.

The spectral response of the camera was also tested with the use of absorbing and scattering epoxy optical phantoms [11] of various optical properties. The reflectance of each phantom was measured using the multi spectral camera. The images were normalized by the values obtained with a white 99.8% reflectance standard. The exposure time and light intensity was kept the same for all the acquisitions. Normalized reflectance at each pixel in the image was calculated with the following expression

$$R(x, y, \lambda) = A \times \frac{R_{phantom}(x, y, \lambda) - Dark(x, y, \lambda)}{R_{whiteSTD}(x, y, \lambda) - Dark(x, y, \lambda)} \quad (1)$$

$R_{phantom}$  is the reflectance of the phantom;  $R_{whiteSTD}$  is the reflectance of the white standard. Dark is an image acquired in complete darkness and it is related to the electrical noise of the camera.  $A$  is a multiplication factor used to take into account the instrument collection efficiency. A region of interest (ROI) of 100 pixels x 100 pixels was cropped from each sub-image. The mean and standard deviation of the ROI was calculated and plotted versus the wavelength. The distance from phantom to the camera was 10 cm. Monte Carlo simulations were used to calculate the reflectance of the phantoms based on their known optical properties [12]. Each simulation was conducted with 1,000,000 photons. Moffit *et al.* [11] indicated in their work that three fourth (3/4) of 112 TiO<sub>2</sub> particles were between 250 and 400 nm in

diameter. Related to these values, they showed anisotropy  $g = 0.51$  at 690nm and  $g = 0.52$  at 830 nm. Values of  $g$  for all other wavelengths of interest were obtained by linear interpolation of the two aforementioned values. The results of this test are shown in Fig. 2; the Monte Carlo simulations support the experiments results. Due to instrumentation limitation the optical properties for phantoms were available only up to the wavelength 850 nm.

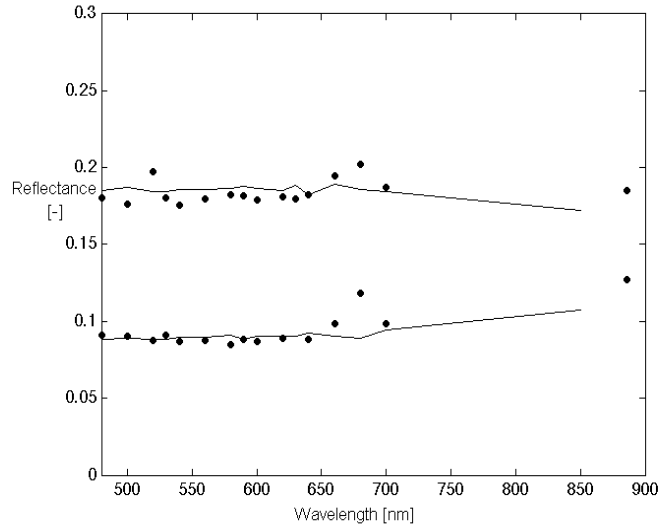


Fig. 2. Comparison between the experiment result and Monte Carlo simulation for 3 epoxy phantoms. The solid black lines represent the Monte Carlo results, the void symbols are the corresponding experimental results. The factor  $A$  was kept constant in all experimental results. Top phantom  $\mu_a = 0.0671 \text{ mm}^{-1}$ ,  $\mu_s' = 0.3464 \text{ mm}^{-1}$ , bottom line  $\mu_a = 0.846 \text{ mm}^{-1}$ ,  $\mu_s' = 1.3175 \text{ mm}^{-1}$  in wavelength 660 nm.

In a second test, reflection of NIST traceable Spectralon standards (Labsphere, North Sutton, NH) of different colors (yellow, red, and green) was measured. The exposure time was adjusted by taking an image of a white standard of 99.8% reflectance to never exceed saturation levels, and was kept the same for all the color standards. An image of a white 99.8% reflectance standard was used once again to normalize the images. A region of interest (ROI) of 50 pixels x 50 pixels was cropped from each sub-image. The mean and standard deviation of the ROI was calculated and plotted versus wavelength.

The result from the reflectance experiment and the color standard data provided by NIST are shown in Fig. 3, once again the camera is able to capture the calibrated reflectance spectrum of a standard element, although some variation is visible at the longest wavelengths, this is due to the spectral shape of our light source and low light level above 700 nm.

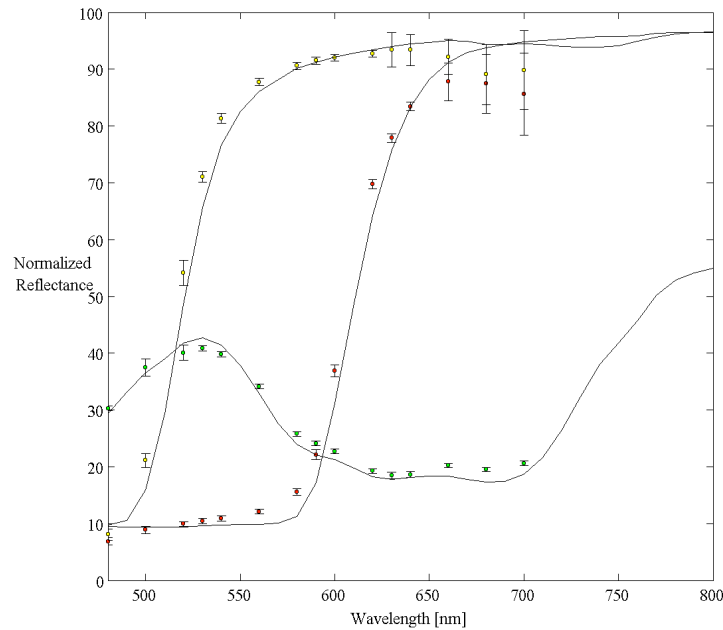


Fig. 3. Reflectance of Spectralon color (green, red, yellow) standard collected by camera compared with calibrated NIST values. Calibrated data is not available above 800 nm, hence the last image of the spectral camera is omitted from this graph.

## 2.2. Distortion

In our multi-spectral camera, each lens sees a slightly different portion of the object of interest, moreover the object is seen by each lens at a slightly different angle. The angular differences cause some angular aberration for each image of each lens. This effect can be referred to as parallax.

Some distortion due to parallax was noticeable in the acquired images. A series of tests were conducted aimed at reducing this effect, first the range of distances between object and camera that caused minimal distortion were studied, in a second set of tests elastic registration of the images was conducted to eliminate the distortion.

A standard imaging sample consisting of a black cross was drawn using Matlab<sup>®</sup> (the Mathworks Inc, Natick, MA). Figure 4 shows the image of the standard image.

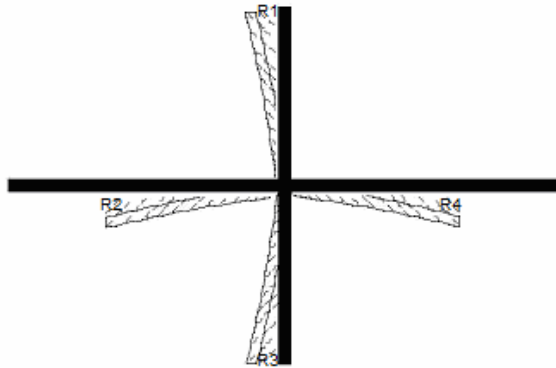


Fig. 4. The thick black line is the standard image used to correct for distortion artifacts. The thickness of each line is 0.6 cm, the vertical line is 14.2 cm and the horizontal line is 21.6cm. The light lines represent a possible distortion observed with the multi-spectral camera. The dashed lines represent the area calculated to assess the level of distortion.

This image was located in different distances from the camera in the range of 5 cm to 14 cm in steps of 0.5 cm, results of the experiment are shown in Fig 5.

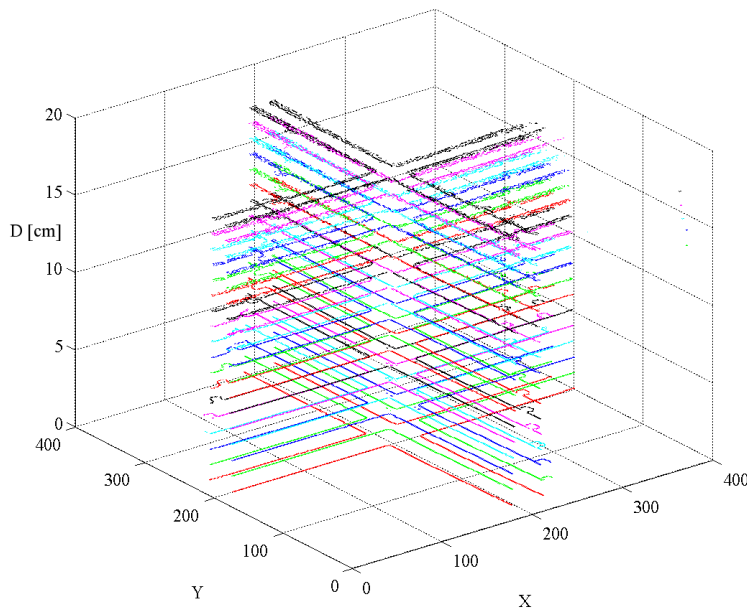


Fig. 5. Images acquired at different target to camera distances (D) for upper left lens in multispectral camera.

As camera to target distance increased two main parameters came into play, image distortion and image magnification. An algorithm was used for calculating distortion. First the number of pixels between the sample image and the image from the camera was calculated  $(R1 + R2 + R3 + R4)$  [pixel x pixel]. Then this factor was divided by the magnification ( $M$ ), which is the number of pixels represented by one centimeter [pixel/cm]. Hence distortion is calculated as

$$Distortion = \frac{R_1 + R_2 + R_3 + R_4}{M} = \frac{[pixel] \cdot [pixel]}{[pixel]/[cm]} = [pixel.cm] \quad (2)$$

In Fig. 6, distortion for 7 different lenses at different distances is shown. It is clear from this graph that in the range of 8.5 to 11.5 cm distortion is at a minimum.

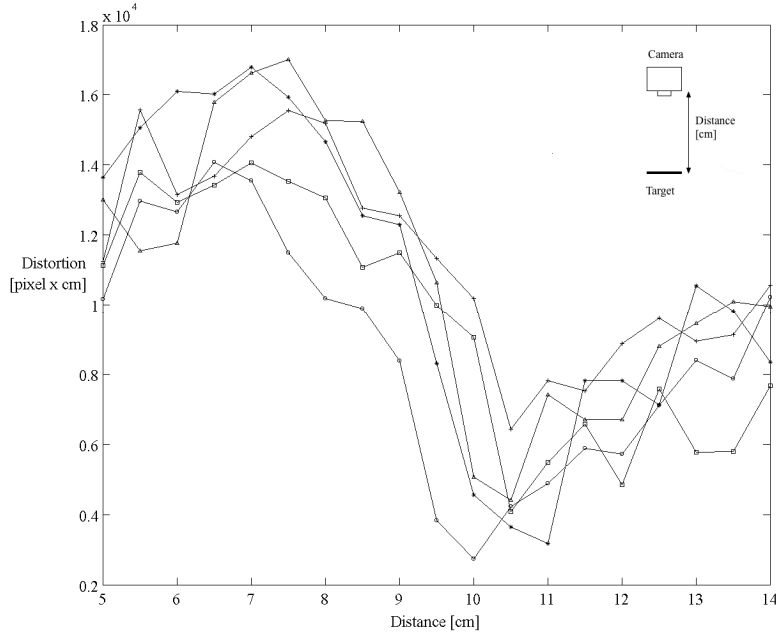


Fig. 6. Calculated distortion at different target to camera distances. The distortion is minimum between 8.5 cm to 11.5 cm for all 7 lenses.

Distortion was also calculated for 1 specific camera-to-target distance for all 18 different wavelength images, although some variation existed within the same snapshot images it was negligible compared to the effect obtained by changing the camera to target distance.

Image registration software, (Match, Medical Technology and Clinical Physics, UMC Utrecht, Netherlands [3,4]) that allows for elastic image registration was ultimately used to minimize the distortion effect on the images. The image obtained with the 540 nm filter was used as the reference image in the software, an affine transformation matrix and a correlation measure based on image gradients was finally used on all the remaining images, only one iteration was conducted for this test and during subsequent analysis. Figure 7 shows the effect on distortion of the Match program.

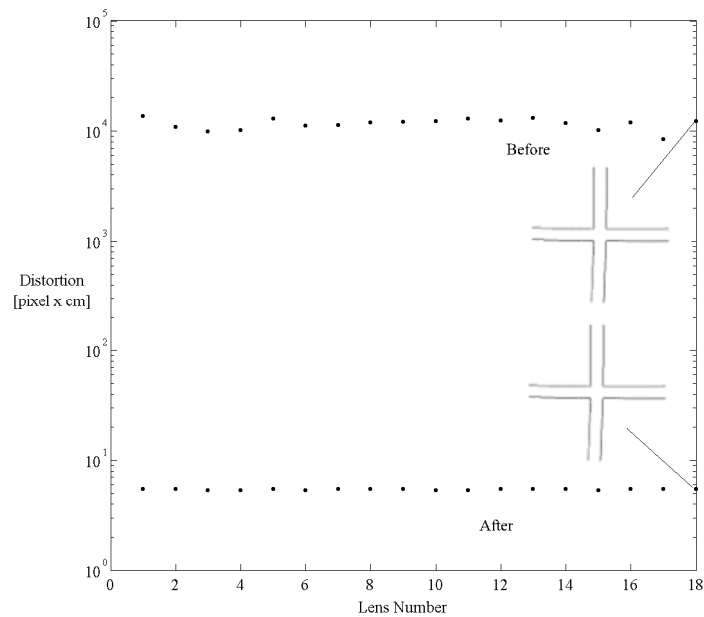


Fig. 7. Blue dots shows the distortion for 18 different lenses at 9.5 cm, and the black dots shows the same distortion after registration.

Once the images were registered the distortion is reduced to levels close to zero.

### 2.3. Preliminary In Vivo Testing

Testing on human skin under hypoxic and ischemic conditions was conducted. A pressure cuff was inflated to 140 mmHg of pressure in order to impede blood circulation to a volunteer arm. The cuff was inflated for duration of 220 seconds and then pressure was released. Figure 8 shows the results at time 0 (prior to inflation) and then 6 different time intervals when the pressure cuff was inflated. At  $t = 240$  seconds the pressure was released when the cuff was opened, monitoring was continued for 4 additional time intervals. A model by Stamata et al. [2,13] was used to produce the oxygen saturation maps of the volunteer hand. The total absorbance curve of skin was corrected for melanin absorption by subtracting its contribution from the general data. Skin pigmentation was approximated as the slope of the fitted straight line between the values of absorbance at 620 nm and 720 nm, the absorbance curve of melanin decreasing monotonically between 600 nm and 750 nm. Oxygen saturation was calculated by using tabulated absorption values of oxygenated and deoxygenated hemoglobin to fit the experimental data in the range 550 nm to 580 nm. In this range both curves exhibit local maxima [13]. The generation of oxygen saturation map was achieved following a model introduced by Stamatas et al. [2] that will be briefly summarized here. Each pixel in the reflectance images obtained with the multi-spectral camera was used to generate curves of reflectance versus wavelength. The data was normalized by values of reflectance obtained with a 99% NIST traceable reflectance standard. Absorbance was calculated by taking the logarithm based 10 of the normalized reflectance. Following this step the effect of melanin absorption and scattering is calculated by fitting values of absorbance in between 630 to 700 nm, and then extrapolating the resulting curve to lower regions of the spectrum. This approximation is appropriate since in the 630 – 700 nm region skin melanin absorption and scattering dominates ( $\mu_{\text{melanin}} = 20$  and  $30 \text{ cm}^{-1}$  [14]  $\mu_{\text{ablood}} = 0.0851$  and  $0.196 \text{ cm}^{-1}$  for 70% oxygenated whole blood [15]).

The resulting curve is subtracted from total values of absorbance; finally a two wavelengths algorithm is used to calculate oxygen saturation from the corrected curve. The algorithm is based on tabulated data of oxygenated and deoxygenated hemoglobin [15]. In this paper (560 nm, 580 nm) were used.

Results of the in-vivo test are shown in the figure below.

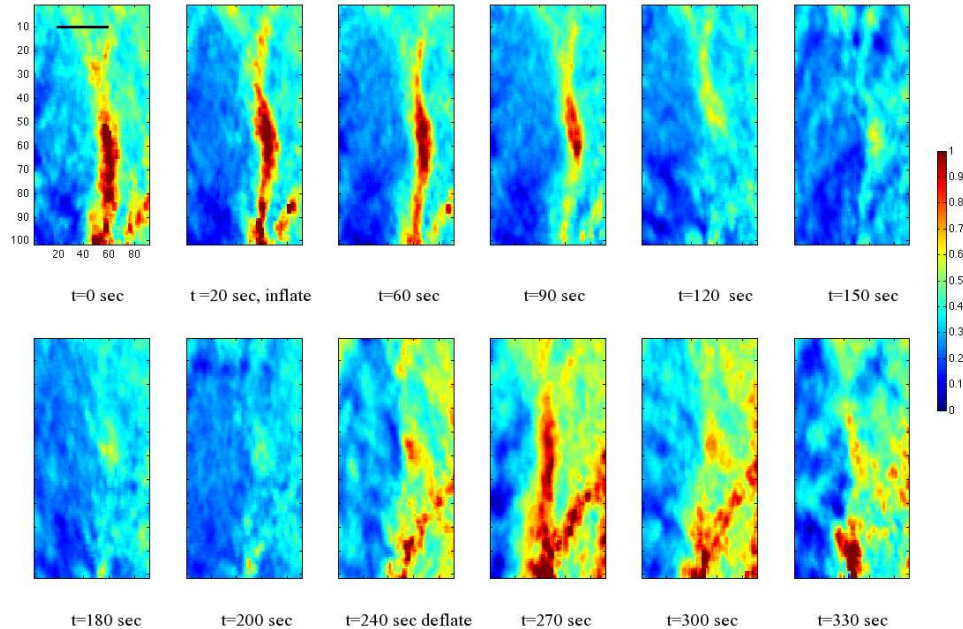


Fig. 8. Oxygen saturation maps ( $SO_2$ ) during the inflation and deflation of a pressure cuff. The false color map relates to oxygen saturation (values are between 0 and 1). The line in the first figure on the left corresponds to 0.5 cm.

The images show a clear relation in between cuff inflation and oxygen saturation. Oxygen saturation increased dramatically when the cuff was removed. The bright lines in the images were superficial arteries in the patient arm.

#### 2.4. Clinical Protocol

The spectroscopic camera described above was utilized in a clinical trial assessing the impact of CACIPLIQ20® on wound healing. CACIPLIQ20® is a medical application containing heparan sulfate, a sugar molecule found naturally in the skin and associated with polypeptides that are involved in wound healing. CACIPLIQ20® replaces sugar molecules that are damaged as a result of skin breakdown, thereby facilitating wound healing.

A study was conducted at National Rehabilitation Hospital (NRH, Washington, DC), which included 15 participants (22 total wounds) with either a pressure ulcer, a diabetic ulcer, a vascular ulcer, or a post surgical wound. All subjects were required to sign an informed consent approved by the Institutional Review Boards of MedStar Research Institute and The Catholic University of America. The wounds were derided, and free of infection before CACIPLIQ20® application. Twice per week CACIPLIQ20®-soaked gauze was applied to the wound bed for 5 minutes. The initial study length was 4 weeks (8 treatments), plus two follow up sessions without treatment. Evaluation of the wounds was conducted weekly via the standardized PUSH tool, VERG digital camera assessment, and multi-spectral camera assessment. The assessment of size obtained with the PUSH and VERG tools were used as indicators of wound healing and were compared to the results obtained with the multi-spectral camera.

### 2.5 PUSH Tool

The Pressure Ulcer Scale for Healing (PUSH) tool is a clinical tool developed by the National Pressure Ulcer Advisory Panel to monitor wound healing. The PUSH tool has the clinician assign numeric values to three main elements: (1) surface area measured by length X width (possible score range of 0-10), (2) amount of exudates (possible score range of 0-4), and (3) tissue type (possible score range of 0-4). Tissue type is a parameter that describes material in the wound, including necrotic tissue.

The wound is given a total score ranging from 0 to 17, with a score of 0 representing a healed wound. Each week, before applying CACIPLIQ20® the study personnel measured the length and width of the wound manually and recorded the values using the PUSH tool describing wounds for each subject. The greatest length (head to toe) and greatest width (side to side) of the wound were measured using a ruler. Recorded scores at each subsequent session were compared with values from previous sessions so as to monitor healing trends.

Digital images were processed using the VERG digital wound measurement system and were used to trace and measure wound dimensions. Images of the wounds were acquired using a commercially available digital camera (PowerShot G9, Canon U.S.A., Inc). The system included a 3 cm x 3 cm white square standard which was placed next to the wound while acquiring the images and was used for calibration. The VERG software package then allows quantification of wound size by tracing length, width, and area on the digital image.

Spectral images of selected wavelengths provided the necessary information for generating maps of skin oxygen saturation. The algorithm described in the calibration section of this paper was used to analyze the data. The algorithm used the curve of absorbance of skin, which is simply the logarithm of the ratio of the skin diffused reflectance to a reflectance standard.

### 3. Results

A typical raw image of a skin wound acquired with our system is shown in Fig. 9, while a typical SO<sub>2</sub> map is shown in Fig. 10. Images were taken in a completely dark room. Patients were asked to sit or lie depending on the location of the wound. Camera exposure time was adjusted to never exceed saturation levels. Generally exposure time was below 500 msec. A disposable paper ruler was placed next to the wound to help in image registration. Images of a 99.8% reflectance standard were acquired at the end of the imaging session and were used for normalization. The images acquired with the spectral camera were processed and results of oxygen saturation were compared to the PUSH score and VERG digital wound measurements. In each session all dressing and bandages were removed and wounds were cleaned using saline. Study personnel recorded any changes from the previous session. After these procedures, a sterile gauze soaked with CACIPLIQ20® was placed on the wound for 5 minutes.

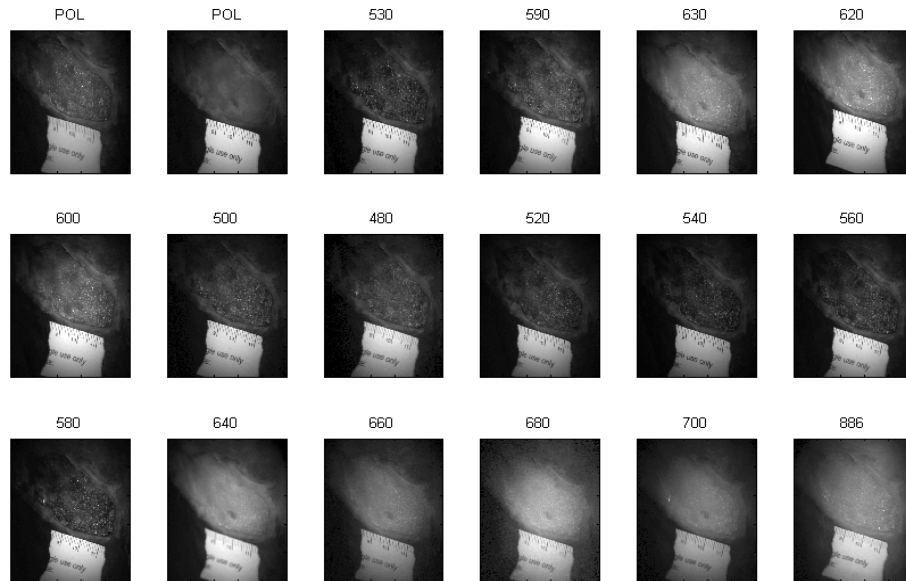


Fig. 9. Typical image acquired with the spectral camera.

To analyze change over time in wound condition the following statistical methods were used: 1) a parametric paired t-test aimed at comparison of study parameters measured via a standardized PUSH tool at the baseline and at the end of treatment; 2) non-parametric Wilcoxon Rank Test allowing comparison between variables with non-normal distribution (e.g., VERG assessment and spectroscopic parameters); and 3) non-parametric repeated measures Friedman ANOVA and General Linear Model (GLM) methods aimed at analyzing change in wound condition during treatment period from session 1 to session 14.

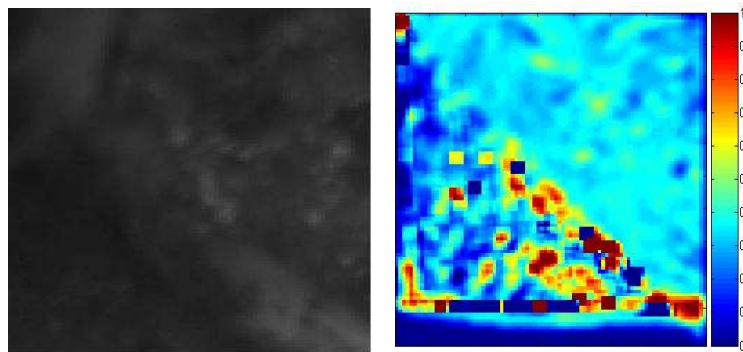


Fig. 10. A typical raw image of the wound at 540 nm, (left) and corresponding oxygen saturation map (right).

Great variability both in wound size and oxygen saturation was observed during the study and was due in part to the patient's initial wound condition, as well as health risk behaviors. For example, 56% of the study participants were identified as smokers, and smoking has been shown to impair wound healing due to nicotine induced narrowing of blood vessels [16].

To analyze trends describing wound healing process over time statistical analysis of the oxygen saturation and wound size as measures by both PUSH and VERG tools was conducted on the 15 patients with 22 wounds (several patients were treated for two different wounds).

All data included in the analysis (10 patients) were of those patients with complete data (at least 8 treatment sessions), including values of oxygen saturation, wound size, and condition.

Paired t-tests were used to assess the change in wound condition measured via the PUSH total score, which improved during the treatment period from 12.06 to 10.44 weeks (P-value = 0.009), representing a 13.4% decrease.

A Wilcoxon Rank Test was used to analyze the wound area measured via the VERG image recognition algorithm. The results show a trend (not statistically significant) toward a decrease by 10% in the size of the treated wound area over time, from session 1 to session 8 (F-value in Wilcoxon rank test = 1.7, P-value = 0.083).

Oxygen saturation values (SO<sub>2</sub>) were analyzed using a parametric t-test, repeated measures General Linear Model (GLM) and non-parametric mean comparison (Wilcoxon criteria and Friedman test) to identify baseline versus treatment change in wound condition. The parametric t-test shows a significant decrease in the oxygen saturation value thus demonstrating a wound dynamic that relates to the above described traditional clinical methods for monitoring healing based on PUSH and VERG tools (Paired T-test value = 4.53, P-value = 0.0001).

A non-parametric analysis of oxygen saturation values (SO<sub>2</sub>) using Wilcoxon criteria and repeated measures Friedman ANOVA, as well as repeated measures General Linear Model (GLM) confirms a significant trend in the reduction of oxygen saturation following a wound healing process from session 1 to session 14, (Z-value in Wilcoxon rank test = 3.0, P-value = 0.003), (F-value in Friedman Test = 12.82, P-value = 0.012), GLM F-value = 21.7, P-value = 0.0001).

#### 4. Discussion

It has been shown that ischemic and hypoxic conditions are detrimental to many different types of wounds [17] hence monitoring of tissue oxygenation during healing could be an important metric in establishing efficacy in wound treatment and care. Fiber based techniques are able to probe skin optical properties at different depths but results are very localized and at times influenced by contact induced ischemia. Imaging spectroscopy is a promising technique for assessment of skin optical properties and non-invasive monitoring of wound healing. When using the range of visible wavelengths shown in this paper only shallow penetration (~1 mm) is to be expected [5], in our clinical trial, none of the skin lesions included an epidermal layer and several of the wounds spanned the deep dermis hence reducing the impact of scattering and absorption due to those superficial structures. The model used in this paper has been successfully used by other authors in the assessment of skin erythema and damage, in our experience it has the advantage of being less prone to artifacts typical of more complex models that rely on the curves of absorption and scattering of the skin most common chromophores [1,3,6], nevertheless we acknowledge that work remains to be done to achieve truly quantitative values of SO<sub>2</sub> and that the results shown here are to be considered as trends or relative to starting conditions.

Our imager has the advantage of capturing images in one snapshot, hence minimizing acquisition time, movement artifacts, and registration requirements, on the other hand it relies on large format camera that are at costly, and not particularly sensitive to low light conditions, moreover the resolution of the images is fairly poor compared to time dependent imagers that can rely on the full CCD.

Wound spectral imaging has the potential to augment the clinical care of people with wounds. We have introduced a new multi-spectral camera system capable of generating maps of oxygen saturation of a wound. Maps of healthy skin obtained with this system show values comparable to the one reported in the literature [2,3,5]. Although only oxygen saturation was reported in this paper other parameters such as water content, melanin concentration, and hematocrit could also be measured with models similar to the one presented here, and could be used for diagnosis of pigmented cancer lesions, burn progress, or monitoring erythema.

Our snapshot imager has the advantage of being immune to movement artifacts but it sacrifices resolution by dividing a large format image into 18 smaller units, therefore we are currently conducting further studies aimed at establishing the minimal number of wavelengths necessary for an accurate assessment of the metrics of interest.

The clinical trial conducted at the National Rehabilitation Hospital on different types of skin ulcers showed that oxygen plays a role during the healing process. In our study oxygen and wound size both decrease with time thus reflecting different aspects of the wound healing process which correlation requires further exploration. The CACIPLIQ20® drug used in the study could be partly responsible for this effect, we acknowledge the fact that given the variability in wound size, type, large variability in the results was to be expected.

### **Acknowledgement**

We gratefully acknowledge the help of Paul Lemaillet and Yuan Liu (Ai).